JOURNAL OF COMPUTATIONAL PHYSICS 70, 89–116 (1987)

Hybrid Simulation of Ion Beams in Background Plasma

A. MANKOFSKY* AND R. N. SUDAN

Laboratory of Plasma Studies, Cornell University, Ithaca, New York 14853

AND

J. DENAVIT

Lawrence Livermore National Laboratory, Livermore, California 94550

Received October 11, 1985; revised June 16, 1986

We present a $2\frac{1}{2}$-dimensional ($r, z, v_r, v_\theta, v_z; \partial/\partial\theta = 0$) quasineutral hybrid code suitable for studying a broad class of plasma and beam-plasma configurations. Ions are represented by particles and electrons by an inertialess thermal fluid which obeys a generalized Ohm's law. Fields are solved in the quasineutral Darwin approximation. Several collisional and atomic processes are also included in the model. The code has been applied to the problem of propagation of intense ion beams through preformed z-pinch plasma channels, a scenario of interest for inertial confinement fusion devices.

1. INTRODUCTION

The past several years have seen quasineutral hybrid (particle-fluid) simulation techniques emerge as powerful tools for the study of complex plasma phenomena occurring over temporal scales which are long compared to the electron plasma period (ω_{pe}^{-1}) and gyroperiod (Ω_{ce}^{-1}) and spatial scales which are long compared to the electron Larmor radius (r_{L_e}). In particular, hybrid models are well suited to problems dominated by the time scales of ion physics, in which case the detailed dynamics of the electron motion are unimportant. Electrons may then be described by an appropriately chosen set of fluid equations, while ions are represented by particles to retain kinetic effects. In addition, if the phenomena of interest are of sufficiently low frequency so that $4\pi|\mathbf{J}| \gg |\partial\mathbf{E}/\partial t|$, the effects of electromagnetic radiation may be neglected in the field equations.

Some of the earliest quasineutral hybrid simulations were performed by Sgro and Nielson [1] in their study of theta-pinch implosions. These simulations were one-dimensional, and attempted to predict experimental pinch results via the inclusion

* Present address: Science Applications International Corporation, McLean, Virginia 22102.

0021-9991/87 $3.00

of anomalous transport coefficients in the equations of motion. The density and magnetic field profiles generated by the simulations were found to be comparable to the profiles obtained from the *ZT*-1 experiment at Los Alamos.

Fundamental numerical stability analyses of quasineutral hybrid models and their extension to multidimensional problems were performed by Byers *et al.* [2]. Both linearized and fully nonlinear models were considered. These simulations were successfully applied to the study of various plasma microinstabilities and to the problem of beam-driven plasma return currents across a magnetic field. The algorithm of Byers *et al.* has been extended by Harned [3] to allow for plasma-vacuum interfaces of arbitrary shape. This model was successfully applied to studies of kink instabilities in long ion layers and rotational instabilities in theta pinches.

A multidimensional hybrid model in which electron inertial effects were retained on the Ω_{ce}^{-1} time scale but excluded on the ω_{pe}^{-1} time scale was developed by Hewett and Nielson [4]. In this way, phenomena requiring finite electron cyclotron frequency could be studied without necessitating the use of a time step small enough to resolve electron plasma oscillations. The code was used to simulate lower hybrid drift instabilities in strongly inhomogeneous plasmas; good agreement with full particle simulations was observed.

Hewett [5] has developed a $2\frac{1}{2}$-dimensional hybrid model with a nearly implicit electron-field algorithm, thereby allowing low density or vacuum regions to develop in simulations without an adverse effect on numerical stability. The exceptional stability properties of the algorithm were demonstrated by the simulation of various pinch implosions.

A linearized hybrid model with fully three-dimensional first-order perturbations was developed by Friedman *et al.* [6] for the study of field-reversed ion rings and mirror plasmas. This code followed the temporal development of a linearized perturbation of specified azimuthal mode number about an axisymmetric equilibrium. Beam ions were treated kinetically, with background ions and electrons represented by individual sets of fluid equations. The model has been used to verify previous analytic results regarding kink and precessional instabilities, and has confirmed the existence of a "tilting" instability in weak ring-plasma systems.

In the present paper we describe a $2\frac{1}{2}$-dimensional quasineutral hybrid model which is suitable for studying the dynamics of intense ion beams and rings in background plasma [7]. Among the new features of the model are: (1) an arbitrary number of ion beam species of arbitrary charge-to-mass ratio; (2) an implementation of the algorithm of Byers *et al.* [2] in axisymmetric $r-z$ geometry ($\partial/\partial\theta = 0$); (3) slowing-down and pitch-angle scattering collisions in both ion and electron equations of motion; (4) finite pressure corrections in the electron equation of motion; (5) a transport equation for electron energy, including sources and sinks of heat in the regime $\nu_s^{ei}/\Omega_{ce} \gg 1$ (ν_s^{ei} is the electron–ion slowing-down collision frequency); (6) a neutral specie modeled by a stationary fluid, including ionization and recombination; and (7) energy loss due to impurity species in coronal equilibrium in an optically thin plasma. The code built from this model, CIDER (Cornell Ion Dynamics and Electron Response), has been successfully applied to

the problem of propagation of intense ion beams through preformed z-pinch plasma channels [8], a scenario of current interest to the inertial confinement fusion community.

The paper is organized as follows. The CIDER model is described in Section 2. Individual subsections are devoted to major pieces of the code, including ions, electrons, transport equations, radiation, field equations, atomic physics, and calculation of collision frequencies. The algorithm used to solve these equations is presented in Section 3. In Section 4 we discuss the detailed testing performed to verify the proper operation of various parts of the code. Finally, a summary and concluding remarks appear in Section 5.

2. Model

2.1. *Ions*

All ion species, respresenting either background or beam ions, are represented by finite-size particles of specified charge-to-mass ratio, and obey Newton's equations of motion,

$$\begin{aligned} \frac{d\mathbf{x}_k}{dt} &= \mathbf{v}_k, \\ \frac{d\mathbf{v}_k}{dt} &= \frac{Z_k e}{m_k}\left(\mathbf{E} + \frac{1}{c}\mathbf{v}_k \times \mathbf{B}\right) - \nu_s^{ie}(\mathbf{v}_k - \mathbf{v}_e) - \nu_s^{io}\mathbf{v}_k, \end{aligned} \tag{1}$$

where the subscript k denotes a particle index and Gaussian units are used.

An arbitrary number of beam ion species can be considered, with a single background ion specie. The code differentiates between beam and background particles for initial conditions, boundary conditions, and for the evaluation of collision terms. The slowing-down collision frequency between incident specie α and field specie β is denoted by $\nu_s^{\alpha\beta}$ [9, 10], and o, i, e, and b denote neutral, background ion, electron, and beam ion quantities, respectively. This representation of the slowing-down effect of collisions is justified in the two limits $|\mathbf{v}_k| \ll v_{th_e}$ and $|\mathbf{v}_k| \gg v_{th_e}$, where v_{th_e} denotes the electron thermal velocity. Its application in the regime $|\mathbf{v}_k| \sim v_{th_e}$ needs to be checked for individual cases. Thus, the three terms on the right-hand side of Eqs. (1) represent, respectively, the Lorentz force, the slowing-down due to collisions with background electrons, and the slowing-down due to collisions with stationary background neutrals. Slowing-down due to ion–ion collisions is not included here since $\nu_s^{ii}/\nu_s^{ie} \sim O(m_e/m_i)$. Ion collisions with a massless electron fluid and with a fixed background specie do not conserve momentum. Energy is not conserved in ion-background collisions; however, the electrons can be heated and energy is conserved in ion–electron collisions. Transverse diffusion of beam ions due to scattering by electrons is not represented in Eqs. (1) but is included in the computations by a Monte Carlo technique. A random energy-

conserving rotation is applied to the velocity vector at each time step, the angle of rotation being proportional to the transverse scattering frequency $\nu_\perp$ [10]. Transverse diffusion of beam ions due to ion–ion collisions is not included.

Note that the retention of the quantity $Z_k e/m_k$ for each group of particles makes it possible to simulate systems in which several species of ions are present.

2.2. *Electrons*

In the present code, we are not interested in phenomena occurring on the time scales of the electron plasma frequency, ω_{pe}, or the electron gyrofrequency, Ω_{ce}. Similarly, we are not interested in the spatial scales of the Debye length, λ_D, or the electron gyroradius, r_{L_e}. In this regime, electron momentum may be neglected by setting the left-hand side of the electron momentum equation to zero,

$$0 = ne\left(\mathbf{E} + \frac{1}{c}\mathbf{v}_e \times \mathbf{B}\right) + \nabla p_e + nm_e\left[\sum_\alpha \nu_s^{e\alpha}(\mathbf{v}_e - \mathbf{v}_\alpha) + \nu_s^{eo}\mathbf{v}_e\right]. \tag{2}$$

Here, $\mathbf{v}_\alpha$ represents the local mean velocity of ion specie α. The electron pressure is given by

$$p_e = nT_e, \tag{3}$$

and we have used quasineutrality,

$$n_e \approx \sum_\alpha Z_\alpha n_\alpha \equiv n. \tag{4}$$

2.3. *Energy Transport*

The electron temperature is determined from [11]

$$\frac{3}{2}n\frac{dT_e}{dt} + p_e\nabla\cdot\mathbf{v}_e = -\nabla\cdot\mathbf{q}_e + Q_e. \tag{5}$$

In Eq. (5), $d/dt \equiv \partial/\partial t + \mathbf{v}_e\cdot\nabla$, $\mathbf{q}_e$ is the electron heat flux, and Q_e is the electron heating term. The specific forms for $\mathbf{q}_e$ and Q_e depend on the physics being included in the model. At present, we assume the electrons to be highly collisional (i.e., $\Omega_{ce}\tau_e \ll 1$, where τ_e is the characteristic electron collision time). The electron heat flux then takes the form

$$\mathbf{q}_e = anT_e\mathbf{u} - \kappa\nabla T_e, \tag{6}$$

where a is a numerical factor depending only on the charge state Z of the specie involved, $\mathbf{u} \equiv \mathbf{v}_e - \mathbf{v}_i$ is the relative streaming velocity, $\mathbf{v}_i$ is the mean background ion velocity, and the electron thermal conductivity is given by

$$\kappa \equiv b\frac{nT_e}{\nu_s^{ei}m_e}. \tag{7}$$

Again, the numerical factor b is a function only of Z. For the electron heating term Q_e, we take

$$Q_e = \frac{3m_e}{m_i} \nu_s^{ei} n(T_i - T_e) + \eta J_{\text{plasma}}^2 - \frac{a}{e} \mathbf{J}_{\text{plasma}} \cdot \nabla T_e$$
$$+ \frac{\gamma - 1}{2} \nu_\varepsilon m_b \langle v_b^2 \rangle n_b - R. \tag{8}$$

In Eq. (8), the terms represent temperature equilibration with the background ions, return current heating, Thomson effect (thermal gradient) heating, collisional energy deposition due to the beam, and radiational cooling, respectively. Recall that only a single background ion specie is considered, γ is the ratio of specific heats, ν_ε the collisional energy loss frequency, R the radiative cooling term to be discussed below, and η the resistivity, given by

$$\eta \equiv \frac{\nu_s^e m_e}{ne^2}. \tag{9}$$

The superscript e as in ν_s^e denotes a total electron quantity, in this case the total collision frequency, including neutrals.

2.4. *Radiation*

As will be discussed below, the model we have chosen for the fields excludes displacement current, so that a fully self-consistent treatment of radiation is not done here. Such a treatment is not necessary for the slow time scales to be considered, and would introduce the noise and time scale problems commonly associated with electromagnetic codes. However, it is still possible to account for radiational cooling of the electron fluid by introducing the term R in Eq. (8). Several authors [12, 13] have calculated radiational cooling rates due to various impurities in a plasma assumed to be in coronal equilibrium (collisional excitation balanced by radiative decay), including such effects as Bremsstrahlung, recombination, and line radiation. These data are usually presented as polynomial fits, making them ideal for the present application. Thus, we write

$$R \equiv n_0 n L_z,$$
$$\log L_z \equiv \sum_{l=0}^{5} A_l (\log T_e)^l, \tag{10}$$

where n_0 is the neutral or impurity density of the element in question, and the A_l are coefficients taken from the references just mentioned. At present, coefficients for hydrogen, carbon, lithium, oxygen, nitrogen, argon, and gold have been included; the plasma is assumed to be optically thin. Note that the assumption of an ionization equilibrium such as the corona model [14, 15] can break down on short

time scales, but the general results and trends obtained herein should still be of interest.

2.5. *Field Equations*

Since we are interested only in low frequency phenomena such that $4\pi|\mathbf{J}| \gg |\partial\mathbf{E}/\partial t|$, it is appropriate to neglect displacement current by solving Maxwell's equations in the quasineutral Darwin approximation [7, 16–18]. In this approximation, Ampère's law reduces to

$$\nabla \times \mathbf{B} = \frac{4\pi ne}{c}(\langle \mathbf{v}_i \rangle - \mathbf{v}_e), \tag{11}$$

where

$$\langle \mathbf{v}_i \rangle \equiv \frac{\sum_k Z_k n_k \mathbf{v}_k}{\sum_k Z_k n_k}$$

is the charge-averaged velocity of all (background and beam) ions. The code monitors $\delta n/n \equiv \nabla \cdot \mathbf{E}/4\pi ne$ as a check on the validity of the quasineutral approximation; this quantity is never observed to be larger than about 10^{-7}.

Solving Eq. (11) for $\mathbf{v}_e$, substituting into Eq. (2) and rearranging, we find

$$\mathbf{E} = -\frac{1}{c}\left(\langle \mathbf{v}_i \rangle - \frac{c}{4\pi ne}\nabla \times \mathbf{B}\right) \times \mathbf{B} - \frac{1}{ne}\nabla(nT_e)$$
$$-\frac{m_e}{e}\left[\sum_\alpha \nu_s^{e\alpha}\left(\langle \mathbf{v}_i \rangle - \frac{c}{4\pi ne}\nabla \times \mathbf{B} - \mathbf{v}_\alpha\right) + \nu_s^{eo}\left(\langle \mathbf{v}_i \rangle - \frac{c}{4\pi ne}\nabla \times \mathbf{B}\right)\right]. \tag{12}$$

This expression is used to obtain the electric field; the magnetic field is obtained from Faraday's law,

$$\frac{\partial \mathbf{B}}{\partial t} = -c\nabla \times \mathbf{E}. \tag{13}$$

Finally, note that Eq. (11) can also be used to eliminate the electron drift velocity from the collisional term in the ion equation of motion (Eqs. (1)), giving

$$\frac{d\mathbf{v}_k}{dt} = \frac{Z_k e}{m_k}\left(\mathbf{E} + \frac{1}{c}\mathbf{v}_k \times \mathbf{B}\right) - \nu_s^{ie}\left(\mathbf{v}_k - \langle \mathbf{v}_i \rangle + \frac{c}{4\pi ne}\nabla \times \mathbf{B}\right) - \nu_s^{io}\mathbf{v}_k. \tag{14}$$

We have therefore eliminated $\mathbf{v}_e$ from all our equations, leaving everything in terms of field and particle quantities, and the electron temperature. This is the motivation for naming CIDER an ion dynamics and electron response code: the electrons simply respond to the ion dynamics in such a way as to maintain quasineutrality, and contribute to the current supporting the magnetic field.

2.6. *Neutrals and Atomic Physics*

Neutral gas background is modeled as a stationary fluid quantity in CIDER, and therefore makes its presence known only via collisions, ionization, recombination, and radiational cooling of the electron fluid. No attempt is made to follow the motion of the neutral fluid, and presumably the code is applicable to only those situations where the time scales are such that this can be justified.

An optional coronal equilibrium model is also available in CIDER to compute ionization of the background gas. In this model [14, 15], collisional excitation and ionization are balanced by radiative decay, with three-body recombination available if desired. It is assumed here that collisionally-induced changes in the populations of the atomic energy levels occur on time scales long compared with the typical atomic relaxation time $\tau_r \approx 10^{12}/n_e$ sec; see Eq. (30) of Reference [15]. Under these conditions, the equilibrium ion density, for single ionization, is given by

$$\frac{n_i}{n_0} = \frac{S}{\alpha_r + n\alpha_3}, \tag{15}$$

where

$$S \equiv \frac{10^{-5}(T_e/E_\infty^0)^{1/2}}{(E_\infty^0)^{3/2}(6 + T_e/E_\infty^0)} \exp(-E_\infty^0/T_e) \tag{16a}$$

is the ionization coefficient,

$$\alpha_r \equiv 5.2 \times 10^{-14} Z (E_\infty^0/T_e)^{1/2} \times \left[0.43 + \frac{1}{2} \ln \frac{E_\infty^0}{T_e} + 0.469 (E_\infty^0/T_e)^{1/3} \right] \tag{16b}$$

is the radiative recombination coefficient, and

$$\alpha_3 \equiv 8.75 \times 10^{-27} T_e^{-4.5} \tag{16c}$$

is the three-body recombination coefficient for single ionization. Here E_∞^0 is the ionization energy of the specie in question, and temperatures and energies are expressed in electron volts. If the above condition on τ_r is not met, the coupled rate equations of the time-dependent corona model [15] must be solved to obtain the neutral density. This time-dependent model would appear to be more appropriate at some densities, but the numerical solution of the rate equations is a very complex process in its own right. The equilibrium model is a first attempt at including the proper physics.

The implementation of a model such as Eqs. (15) and (16) in a code where ions are represented by particles is nontrivial, and will be discussed below. For now, it is sufficient to say that the neutral density profiles may be either constant in time, or updated at each time step to account for ionization according to Eq. (15).

2.7. *Collision Frequencies*

Slowing-down, transverse diffusion, and energy loss collision frequencies for encounters between charged particles are calculated from the standard Spitzer expressions [9, 10]. In highly collisional parameter regimes, it is sometimes necessary to scale these frequencies by a factor $f_\nu \gtrsim 0.1$. This is necessary because numerical stability and accuracy suffer when the quantity $\nu\Delta t$ becomes much greater than unity. In other words, the particle collision time must be greater than the time step used in the code if collisional effects are to be resolved temporally. Results are then scaled to the fully collisional case $f_\nu = 1$ as discussed in [8].

Charged particle-neutral collision frequencies are calculated differently, depending on the specie in question. For the background plasma, the thermal velocity is assumed greater than the drift velocity, so we take

$$\nu_s^{\alpha o} = n_o \sigma_{o\alpha} (T_\alpha / m_\alpha)^{1/2}, \tag{17}$$

where the cross section $\sigma_{o\alpha}$ is typically about 5×10^{-15} cm^2 [19]. The opposite limit applies to the beam: the drift velocity is assumed greater than the thermal velocity. For protons in various gases, Janni [20] has tabulated values of the energy loss dE/dx as a function of energy. We interpolate linearly between these values, and then compute the collision frequency as follows. Using the chain rule,

$$\frac{dE}{dt} = \frac{dE}{dx}\frac{dx}{dt} = v_b \frac{dE}{dx}; \tag{18}$$

but E denotes the beam particle energy, whence

$$\frac{dE}{dt} = \frac{1}{2} m \frac{d}{dt} v_b^2 = m v_b \frac{dv_b}{dt}. \tag{19}$$

Combining Eqs. (18) and (19) and introducing the definition of the slowing-down frequency, $dv_b/dt = -\nu_s v_b$, gives

$$\nu_s = \frac{-dE/dx}{m v_b}. \tag{20}$$

In a similar fashion, Ziegler and Chu [21] give polynomial fits for energy loss of He^{++} ions in various gases; we again use Eq. (20) to compute collision frequencies from these values. At present, CIDER has provisions for either hydrogen or argon as the background gas.

3. Algorithm

3.1. *Global Timestep*

The global CIDER time advance is a generalized $r-z$ implementation of the predictor–corrector algorithm of Byers *et al.* [2]. Knowing the quantities $\mathbf{E}^{n-1}$,

$\mathbf{B}^{n-1/2}$, $\mathbf{x}_k^n$, $\mathbf{v}_k^{n-1/2}$, and $T_e^{n-1/2}$, where superscripts denote time levels, the time advance may be performed as follows:

(1) Compute $\mathbf{E}^{n-1/2}$ from Eq. (12). Note that this expression involves only one time level. From $\mathbf{E}^{n-1/2} = 1/2(\mathbf{E}^{n-1} + \mathbf{E}^n)$, predict $\mathbf{E}^n_{\text{pred}} = 2\mathbf{E}^{n-1/2} - \mathbf{E}^{n-1}$.

(2) Use Eq. (13) to predict $\mathbf{B}^{n+1/2} = \mathbf{B}^{n-1/2} - c\Delta t \nabla \times \mathbf{E}^n$. Then $\mathbf{B}^n = 1/2(\mathbf{B}^{n-1/2} + \mathbf{B}^{n+1/2})$.

(3) Advance the particles using Eqs. (14) and (1) to obtain $\mathbf{v}_k^{n+1/2}$ and $\mathbf{x}_k^{n+1}$, and compute currents and densities. Volume weighting is used to attribute particle moments. It is sometimes possible to achieve comparable accuracy and shorter running time pushing the particles only once per time step in the *converged* fields [22].

(4) Advance the electron temperature using Eq. (5) and subsequent equations, giving $T_e^{n+1/2}$.

(5) Compute $\mathbf{E}^{n+1/2}$ from Eq. (12).

(6) Obtain a corrected value of $\mathbf{E}^n$, using $\mathbf{E}^n_{\text{corr}} = 1/2(\mathbf{E}^{n-1/2} + \mathbf{E}^{n+1/2})$.

(7) Perform the convergence check,

$$\frac{\max_{i,j} |E_{i,j}^{q+1} - E_{i,j}^q|}{\max_{i,j} |E_{i,j}^q|} \leqslant \varepsilon, \tag{21}$$

for all three components of $\mathbf{E}^n_{\text{corr}}$. Here, q represents an iteration number, and i and j represent cell indices in the z and r directions, respectively. We typically set $\varepsilon = 10^{-6}$, with $3-15$ iterations being required for convergence. If convergence is not achieved, we return to step (2) and begin the next iteration, with $\mathbf{E}^n_{\text{corr}}$ replacing $\mathbf{E}^n$.

Note that it is necessary to enforce a density minimum so as not to violate a Courant condition on the Alfvén speed on the grid. We therefore require that

$$n > \frac{B^2(\Delta t)^2}{4\pi m_i \min(\Delta r^2, \Delta z^2)}, \tag{22}$$

for all grid points. Here m_i is the mass of the background ion specie. Also, collision frequencies are evaluated *explicitly* prior to the beginning of a new time step. While it would be more accurate to compute new collision frequencies during the iteration, it is found that this seriously degrades the convergence of the scheme, probably because yet another variable is free to float. Acceptable results are obtained with the explicit evaluation of collision frequencies. It is also necessary to keep the electron temperature above a critical value T_c in the calculation, to avoid problems encountered in evaluating terms going as $T^{-3/2}$. This value is typically set to 0.1 eV. Furthermore, it is sometimes necessary to apply digital filtering to computed field quantities to lessen the effects of short wavelength noise. Finally, if beam particles are to be injected, quasineutrality is automatically enforced since the electron density is obtained from Eq. (4), which accounts for new particles by construction.

In addition, the iterative procedure used here to solve the electric field equation, Eq. (12), is subject to convergence conditions which are discussed in the Appendix.

3.2. *Particle Pushing Algorithm*

Particle velocities and positions are advanced in a leapfrog fashion using an algorithm originated by Nielson and Lindman [23], modified to operate in $r-z$ geometry and to include collisions. This algorithm is second-order accurate but not fully time-reversible; its empirical stability and accuracy properties are excellent, however. The algorithm is as follows:

$$\mathbf{v}^{n+1/2} = g_1[f\mathbf{v}^{n-1/2} + g_0\mathbf{v}_j + h[\mathbf{E}^n + g_2(\tilde{\mathbf{v}} \times \mathbf{B}^n + g_3\mathbf{B}^n)/c]], \tag{23}$$

$$\mathbf{x}^{n+1} = \mathbf{x}^n + \mathbf{v}^{n+1/2}\,\Delta t, \tag{24}$$

where $h \equiv q\,\Delta t/m$, $g_0 \equiv v\,\Delta t$, $g_1 \equiv 1/(1+g_0)$, $g_2 \equiv 1/(1+g_0/2)$, $g_3 \equiv h(\mathbf{v}^{n-1/2}\cdot\mathbf{B}^n)/2$, $f \equiv 1 - h^2 g_2(\mathbf{B}^n)^2/2$, $\tilde{\mathbf{v}} \equiv \mathbf{v}_*^{n-1/2} + h\mathbf{E}^n/2$, and $\mathbf{v}_*^{n-1/2} \equiv \mathbf{v}^{n-1/2} + g_0\mathbf{v}_j/2$. In Eq. (23), $\mathbf{v}_j$ denotes the fluid velocity of the colliding specie.

To avoid singularities near the system axis, each particle is actually pushed in a local Cartesian system in the $r-\theta$ plane whose origin is located at the particle's position at time n, and whose x-axis lies along the particle's radius vector in the cylindrical system (see Fig. 1). Radial quantities then correspond to x direction, azimuthal quantities to the y direction, and the z direction remains unchanged. After the push is performed, a transformation $(x, y, z) \to (r, \theta, z)$ is applied. Since velocities are defined at half time steps, the identification of their radial component with v_x and azimuthal component with v_y yields a phase error $\simeq \omega\,\Delta t/2$ which causes the force terms in Eq. (23) to lose exact time centering. However, no anomalies have been observed in the tests and applications of the code made thus far.

As mentioned in Section 2.1, CIDER has an option whereby beam ions may

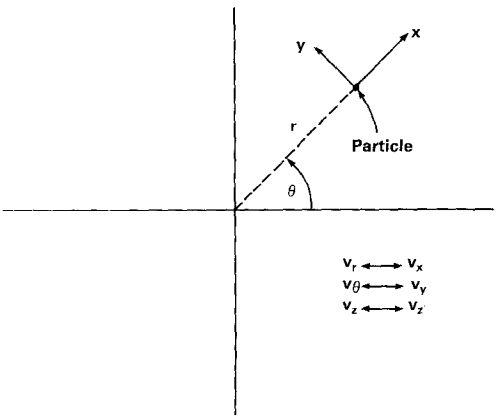

FIG. 1. Coordinate system used in the CIDER particle push.

undergo small-angle, energy conserving scattering events. If this option is selected, each particle's poloidal velocity is rotated through some angle α in the $r-z$ plane after the final push for a given time step (i.e., after the iteration has converged). We determine α as follows. First, the transverse diffusion collision frequency is calculated using the fast asymptotic form of the standard Spitzer expression [19],

$$\nu_{\perp}^{ie} = 1.8 \times 10^{-7} f_{\nu}(m/m_p)^{-1/2} nZ^2 \lambda E^{-3/2}. \tag{25}$$

Here, f_{ν} is the scaling factor discussed in Section 2.7, m_p is the proton mass, λ the Coulomb logarithm, and E the beam ion energy in electron volts. The magnitude of α is then given by

$$|\alpha| = \nu_{\perp}^{ie} \Delta t. \tag{26}$$

Finally, a random sign is assigned to this result, and the particle's velocities are rotated by applying the standard rotation matrix. A similar procedure has been used in Monte Carlo simulations of electron heat flow [24].

3.3. *Electron Temperature Solution*

The electron temperature Eq. (5), is solved implicitly in the terms which are linear in T_e. All other terms (return current heating, collisional heating, the ion part of the equilibration term, and radiational cooling) are treated as source terms. Transport coefficients are also evaluated explicitly. The resulting system of equations (one equation for each interior grid point) is solved by the alternating-direction implicit (ADI) technique.

Even though this approach is as implicit as practicable, negative temperatures are occasionally generated. These nonphysical results are usually due to some combination of stiffness and steep gradients in the equations. The most successful fix for this problem has been simply to clip any negative temperatures, so that $T_e^{n+1/2}$ is replaced by $\max(T_e^{n+1/2}, 0)$ [25]. This approach is reasonable, since negative temperatures are generated by "overshoot": the temperature equation is trying to cool off a hot spot too quickly for the numerics, and extrapolates below zero. Clipping merely prevents the extrapolation from going too far. Results obtained using this approach appear to be quite acceptable, especially since negative temperatures arise infrequently, and then only in a few isolated cells.

3.4. *Corona Model*

If the optional coronal equilibrium model, Eqs. (15) and (16), is to be satisfied at each time step, it is necessary to adjust the background neutral and ion densities accordingly. The neutral density adjustment is easily accomplished because the neutrals are taken to be a fluid quantity. But for the ions, an efficient way of deciding which particles are to be affected by density adjustments must be devised.

CIDER treats this problem as follows. First, a density increment Δn_{ij} is computed for each cell. This increment represents the change in ion density required to satisfy

Eqs. (15) and (16). The corresponding change in neutral density is then $-\Delta n_{ij}$. The particle table is then searched for the one particle closest to the center of the cell. If $\Delta n_{ij} > 0$, that particle's weight is increased accordingly. The corresponding neutral density is decremented by Δn_{ij}, and we continue on to the next cell. If $\Delta n_{ij} < 0$, however, it is possible that the particle closest to the center of the cell does not represent a sufficient number of ions. In this case, we remove a specified fraction of the particle's weight (usually 90%, to avoid generating "null particles" carrying no ions), adjust Δn_{ij}, and search for the next nearest particle. The process is then repeated until either $\Delta n_{ij} = 0$ or we run out of particles in the cell. Finally, the original $-\Delta n_{ij}$ is added to the local neutral density.

There are some difficulties associated with the actual implementation of this technique. Since particles are one cell in size, unless a particle is sitting exactly at the center of a cell it will spill over into adjacent cells. This spillover means that an exact equilibrium will not be generated since the density change due to one particle becomes nonlocal. A similar problem results when $\Delta n_{ij} < 0$ and we run out of particles in that cell. It is found, however, that the equilibria that are actually generated by this algorithm are satisfactory in that smooth profiles accurate to within an order of magnitude of the exact solution are usually obtained. As an example, a test case was run in which 6.77×10^{16} protons of energy 5 MeV were injected into a

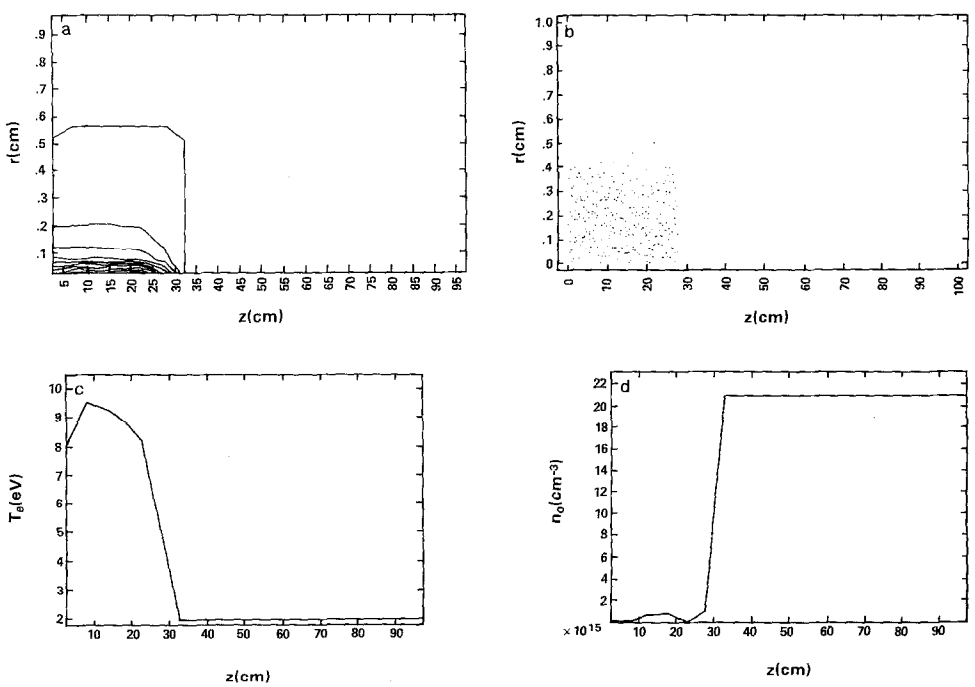

FIG. 2. Corona model test output: (a) beam density contours, (b) beam particle positions; every sixth particle is plotted, (c) T_e versus z at $r = 0.125$ cm, (d) n_0 versus z at $r = 0.125$ cm.

hydrogen plasma channel of density $n_i = 2 \times 10^{18}\ \mathrm{cm}^{-3}$ on axis, electron temperature $T_e = 6$ eV on axis, and neutral density $n_0 = 2 \times 10^{16}\ \mathrm{cm}^{-3}$ on axis. The channel carried 36.5 kA of axial current initially. In Figs. 2 we present several diagnostics showing the state of the system at $t = 10$ nsec. The head of the beam has reached $z \approx 28$ cm, as shown in Figs. 2a, b. The axial profile of electron temperature at $r = 0.125$ cm, Fig. 2c, indicates that $T_e \approx 8$–9 eV in the vicinity of the beam, so we would expect a reduction in neutral density in this region according to Eqs. (15) and (16). Indeed, the axial profile of neutral density at $r = 0.125$ cm in Fig. 2d shows that n_0 has been reduced to about $10^{14}\ \mathrm{cm}^{-3}$ where the beam has heated the plasma. This result compares favorably with the value $n_0 \approx 3.5 \times 10^{13}\ \mathrm{cm}^{-3}$ as computed from Eqs. (15) and (16). The neutral density is seen to be unchanged from its original value in regions which have not yet been heated by the beam. We therefore conclude that the corona model demonstrates the correct semiquantitative behavior.

3.5. *Boundary Conditions*

A variety of field and particle boundary conditions are available in CIDER by setting appropriate guard cell values.

Field boundary conditions at the system axis, $r = 0$, are obtained geometrically by considering the parity of the fields π radians around the cylinder. For example, E_z is continuous across $r = 0$, but E_r changes sign.

The cylindrical wall at radius $r = r_w$ is taken to be perfectly conducting, so that E_θ and E_z must vanish at this wall. To obtain the proper boundary condition on E_r at $r = r_w$, we write Gauss' law in axisymmetric geometry,

$$\nabla \cdot \mathbf{E} = \frac{1}{r}\frac{\partial}{\partial r}(rE_r) + \frac{\partial E_z}{\partial z} = 4\pi\rho. \tag{27}$$

Evaluating this at $r = r_w$ and noting that $E_z(r = r_w) = \rho(r = r_w) = 0$, we find

$$\left.\frac{\partial}{\partial r}(rE_r)\right|_{r = r_w} = 0. \tag{28}$$

Hence rE_r is constant across the wall, giving us the desired boundary condition. Analogous results obtain for the magnetic field if we replace Gauss' law by Ampère's law. Finally, field boundary conditions may be either periodic or perfectly conducting in z.

Particle boundary conditions are reflecting at both $r = 0$ and $r = r_w$. Reflecting, periodic, or absorbing particle boundary conditions may be selected at $z = 0$ and $z = z_{max}$.

3.6. *Implementation and Timing*

CIDER was written specifcally for the CRAY-1 and CRAY X-MP computers and the CTSS operating system. Extensive series of runs on a 22×22 grid with $\varepsilon = 10^{-6}$

in Eq. (21) have shown CPU times of 30–150 μsec/particle/time step, depending on collisionalities, pulse lengths, etc. We have typically used 10,000–15,000 particles and run the code for 500–1000 time steps ($\Delta t = 10^{-11}$–10^{-9} sec), so that a representative run takes about 30 min of machine time. Many of the runs perform diagnostics every 10 or 20 time steps, and it is found that a significant amount of time is spent doing graphics. A longer interval between diagnostics would speed up the code considerably. Turning on the corona model or expanding the grid and/or particle tables so that all the data could no longer be contained in core (necessitating frequent disk I/O) would slow the code down to some extent, but we find CIDER to be an extremely efficient code considering the complexity of the physics model upon which it is built.

4. Code Verification and Testing

A series of verification runs consisting of known test cases was performed to test the numerical stability and accuracy of the code. Following Friedman [6], we have performed two extensive sets of verification runs: normal mode tests and plasma return current simulations.

4.1. *Normal Mode Tests*

These tests consist of exciting linearized normal modes of known dispersion relation and comparing the resulting oscillation frequencies with analytic results. No beam is injected in these runs, but since CIDER treats a beam particle in the same way as any other ion, we can expect this type of test to verify much of the algorithm and coding.

The normal modes of a cold cylindrical plasma in a uniform external field $(0, 0, B_0)$ have been considered by Bernstein and Trehan [26] and by Stix [27]. Friedman [6] has modified these results to include a perfectly conducting outer wall. Letting the perturbed fields vary as $\exp[i(k_\parallel z - \omega t)]$, the two-fluid equations in the limit $\omega/\Omega_{ce} \ll 1$ yield the dispersion relation

$$-\frac{\omega^2}{v_A^2}\mathbf{B} = \nabla \times \left\{ [(\nabla \times \mathbf{B}) \times \hat{z}] \times \hat{z} + i\frac{\omega}{\Omega_{ci}} (\nabla \times \mathbf{B}) \times \hat{z} \right\}, \tag{29}$$

where $v_A = B_0/(4\pi m_i n)^{1/2}$ is the Alfvén velocity and $\Omega_{ci} = eB_0/m_i c$ is the ion cyclotron frequency. The z-component of this equation yields a Bessel equation for B_z, whose solution is

$$B_z = \tilde{B} J_0(\nu r), \tag{30}$$

where $\tilde{B}$ is a constant and ν is given by

$$\nu^2 = -\frac{1}{A^2}\left(1 \Big/ \left(k_\parallel^2 - \frac{\omega^2}{v_A^2} - \frac{k_\parallel^2 \omega^2}{\Omega_{ci}^2}\right)\right), \tag{31}$$

with

$$\frac{1}{A}=\left[k_{\parallel}^2-\frac{\omega^2}{v_A^2}\right]^2-k_{\parallel}^4\frac{\omega^2}{\Omega_{ci}^2}. \tag{32}$$

This expression is substituted back into Eq. (31) and the resulting biquadratic solved to give the wave frequency,

$$\begin{aligned}\omega = v_A\{[\tfrac{1}{2}[v^2(1+\gamma^2)+k_{\parallel}^2(\gamma^2+2)]\\ \pm\tfrac{1}{2}\{[v^2(1+\gamma^2)+k_{\parallel}^2(\gamma^2+2)]^2-4k_{\parallel}^2[v^2+k_{\parallel}^2]\}^{1/2}]\},\end{aligned} \tag{33}$$

where $\gamma \equiv k_{\parallel} v_A/\Omega_{ci}$.

The conducting wall boundary condition $B_r(r_w)=0$ must still be satisfied. Substituting Eq. (30) into the radial component of Eq. (29), this becomes

$$\frac{\partial}{\partial r}J_0(\nu r)\bigg|_{r=r_w} = -J_1(\nu r_w)=0, \tag{34}$$

indicating that there is a discrete spectrum of radial modes. These modes are specified by $\nu_m=\zeta_m/r_w$, where ζ_m is the mth zero of J_1.

To obtain explicit representations for the wave quantities, we first combine Faraday's law and Ampère law to give

$$\nabla\times(\nabla\times\mathbf{E})=\frac{4\pi i\omega}{c^2}\mathbf{J}. \tag{35}$$

Using the fluid equations for $\mathbf{J}$, the radial component of Eq. (35) gives

$$\frac{iE_r}{E_\theta}=\omega^3/\Omega_{ci}^3\Big/\left(\frac{\omega^2}{\Omega_{ci}^2}\left[1+\frac{k_{\parallel}^2c^2}{\omega_p^2}\right]-\frac{k_{\parallel}^2c^2}{\omega_p^2}\right), \tag{36}$$

where $\omega_p=(4\pi nZ_i^2e^2/m_i)^{1/2}$ is the ion plasma frequency. Using this result to eliminate E_r from the azimuthal component of Eq. (35) gives a Bessel equation for E_θ, so that

$$E_\theta=\tilde{E}J_1(\nu_m r), \tag{37}$$

where $\tilde{E}$ is a constant. Expressing all complex exponentials as trigonometric functions, we obtain

$$\begin{aligned}E_r &= |E_r|\cos(k_{\parallel}z-\omega t)\,J_1(\nu_m r),\\ E_\theta &= -|E_\theta|\sin(k_{\parallel}z-\omega t)\,J_1(\nu_m r),\end{aligned} \tag{38}$$

where $|E_r|$ and $|E_\theta|$ are related by Eq. (36). The choices of sines and cosines in

Eq. (38) ensure that E_r and E_θ are out of phase by 90°, as required by Eq. (36). The wave magnetic field can then be obtained from Faraday's law,

$$B_r = \frac{ck_\parallel}{\omega} |E_\theta| \sin(k_\parallel z - \omega t) J_1(v_m r),$$

$$B_\theta = \frac{ck_\parallel}{\omega} |E_r| \cos(k_\parallel z - \omega t) J_1(v_m r), \tag{39}$$

$$B_z = \frac{cv_m}{\omega} |E_\theta| \cos(k_\parallel z - \omega t) J_0(v_m r).$$

Finally, the perturbed current densities are obtained by using Eqs. (38) and (39) in the ion momentum equation, yielding

$$\begin{aligned} J_{i\theta} &= -\frac{\omega_p^2}{4\pi} \frac{\omega}{\Omega_{ci}^2 - \omega^2} \left[-|E_\theta| + \frac{\Omega_{ci}}{\omega} |E_r| \right] \cos(k_\parallel z - \omega t) J_1(v_m r), \\ J_{iz} &= \frac{\omega_p^2}{4\pi} \frac{\omega}{\Omega_{ci}^2 - \omega^2} \left[-\frac{\Omega_{ci}}{\omega} |E_\theta| + |E_r| \right] \sin(k_\parallel z - \omega t) J_1(v_m r). \end{aligned} \tag{40}$$

In the above linearized analysis, we have neglected higher order terms such as $\mathbf{B}^{(1)} \cdot \nabla \mathbf{B}^{(1)}$, where the superscript denotes a perturbed quantity. This approximation is valid if $|\mathbf{B}^{(1)}|/B_0 \ll 1$. From Eqs. (39) and (36) we find

$$\begin{aligned} |\mathbf{B}^{(1)}|/B_0 &\approx \frac{|E_\theta|}{B_0} \left[\frac{c^2 k_\parallel^2}{\omega^2} \left(1 + \frac{|E_r|^2}{|E_\theta|^2} \right) + \frac{c^2 v_m^2}{\omega^2} \right]^{1/2} \\ &= \frac{|E_\theta|}{B_0} \left\{ \frac{c^2 k_\parallel^2}{\omega^2} \left[1 + \left(\omega^3/\Omega_{ci}^3 \Big/ \left(\frac{\omega^2}{\Omega_{ci}^2} \left(1 + \frac{k_\parallel^2 c^2}{\omega_p^2} \right) - \frac{k_\parallel^2 c^2}{\omega_p^2} \right) \right)^2 \right] + \frac{c^2 v_m^2}{\omega^2} \right\}^{1/2} \end{aligned} \tag{41}$$

a quantity which is never larger than about 10^{-7} in the simulations to be described below. Hence the linearized dispersion relation is applicable in the present case. We note, however, that even in the nonlinear regime, Alfvén waves are still found to propagate at the Alfvén velocity v_A [30].

To initialize a given mode, we specify the sign in Eq. (33) (+ for a fast wave, − for a slow wave), the radial mode number m (also called $n_\perp$), the axial mode number $n_\parallel$ (from which $k_\parallel = 2\pi n_\parallel / z_{max}$), and one of the field amplitudes, $|E_\theta|$. We may also interpret $n_\parallel$ and $n_\perp/2$ as the number of axial and radial wavelengths in the mode, respectively. Field quantities are then perturbed using Eqs. (36), (38), and (39) with $t = 0$. Perturbed ion velocities are obtained from Eq. (40) and $\mathbf{J} = nq\mathbf{v}$, since the background ions are taken to be cold. Finally, perturbed electron currents are determined from Ampère's law.

In all our normal mode runs, we take $\Delta t = 1$ nsec, $r_{max} = z_{max} = 4$ cm, $B_0 = 12.5$ kG, $n = 4.62 \times 10^{18}$ cm^{-3}, and $|E_\theta| = 6 \times 10^{-5}$ V/cm. We then have $\Omega_{ci} \Delta t = 0.02$. Eight thousand particles are used on a 22×22 grid (including guard

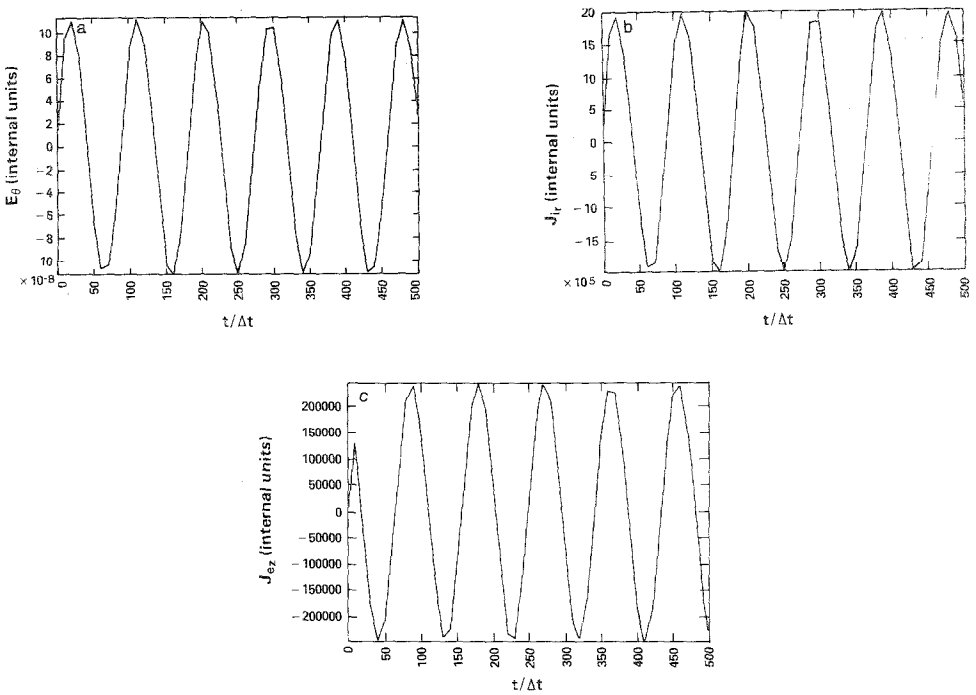

FIG. 3. Normal mode test output at $r = z = 1.7$ cm. The extrema do not appear rounded due to a large diagnostic interval. (a) E_θ versus time, (b) radial ion current density versus time, (c) axial electron current density versus time.

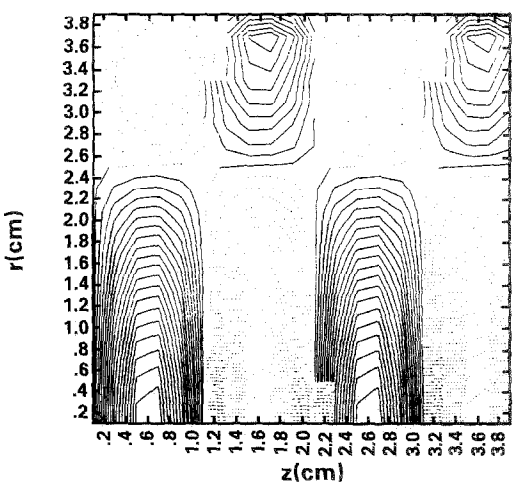

FIG. 4. Spatial mode structure of E_z for a normal mode test run.

cells), so that $\Delta r = \Delta z = 0.2$ cm. The wave is initialized at time step 10. Results from a typical run are presented in Figs. 3. In this run, $n_\perp = 1$, $n_\parallel = 2$, and the upper sign in Eq. (33) was chosen, giving an analytic wave period of 85.5 time steps. The actual wave period as observed in the simulation was 97.8 time steps. As seen in the figures, all quantities—field, ion, and electron—oscillate with this period, indicating proper operation of a major part of the code. The discrepancy between analytic and observed periods is due primarily to finite Δt and Δx effects. Typical spatial mode structure for this run is shown in Fig. 4.

Other normal mode runs are summarized in Table I. In Fig. 5, we present a typical dispersion curve, from which the accuracy of the code as a function of wavelength and frequency may be inferred. It is evident that CIDER performs quite well in regimes where $\omega\Delta t$ or $k\Delta x$ are small. Accuracy decreases as these quantities grow, as evidenced by the increasing differences between numerical and analytic results. However, this effect is well known, and can be controlled by judicious choice of time step and grid spacing.

TABLE I

Summary of Normal Mode Runs

		Analytic		Observed	
$n_\perp$	$n_\parallel$[a]	τ (time steps)	ω/Ω_{ci}	τ (time steps)	ω/Ω_{ci}
1	0	364.4	0.14	369.6	0.14
1	1	176.8	0.30	184.8	0.28
1	2	85.5	0.61	97.8	0.54
1	3	51.7	1.01	65.2	0.80
1	4	34.9	1.50	54.3	0.96
3	0	137.2	0.38	141.3	0.37
3	1	112.6	0.47	119.6	0.44
3	2	73.2	0.72	81.5	0.64
3	3	47.8	1.10	59.8	0.88
3	4	33.3	1.57	54.3	0.96
5	0	84.8	0.62	97.8	0.54
5	1	76.8	0.68	87.0	0.60
5	2	58.9	0.89	76.1	0.69
1	–1	238.5	0.22	239.1	0.22
1	–2	138.1	0.38	152.2	0.34
1	–3	104.1	0.50	119.6	0.44
1	–4	87.3	0.60	108.7	0.48
3	–1	230.4	0.23	228.3	0.23
3	–2	131.1	0.40	141.3	0.37
3	–3	101.0	0.52	108.7	0.48
3	–4	85.9	0.61	103.3	0.51
5	–1	229.1	0.23	228.3	0.23
5	–2	127.1	0.41	135.9	0.39

[a] Sign of $n_\parallel$ is the sign chosen in Eq. (33).

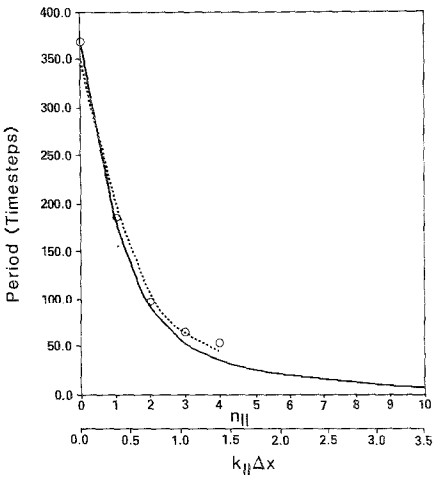

FIG. 5. Typical CIDER dispersion curve, $n_\perp = 1$. The solid line represents the exact theoretical result, the points are code results, and the dashed line is a fit to the code results.

To verify the improved accuracy of the code when the time step is decreased, a run was made in which $n_\perp = 1$, $n_\parallel = 2$, and the time step halved to 0.5 nsec. The observed wave period was 188.8 time steps, or 94.4 equivalent 1 nsec time steps. This represents a 28% reduction in relative error between observed and analytic wave frequencies as compared with the larger time step case.

The collisional terms in the particle and field equations may be tested by observing the damping of a normal mode in the presence of collisions. The observed damping rate may then be compared with the theoretical value, $\gamma \approx \eta c^2 \omega^2 / 8\pi v_A^2$, where η is the plasma resistivity (obtained under the assumption $\omega/\Omega_{ci} \ll 1$). In Figs. 6 we present the results of a run in which all parameters were identical to those in the run of Figs. 3 except that we set $2\pi\nu_s^{ei}/\Omega_{ci} = 0.5$. The observed wave period is unchanged, and the wave is seen to damp with damping rate $\gamma_{observed} \approx 3 \times 10^6$ scc^{-1}. This may be compared with the theoretical value of 7.5×10^5 sec^{-1}. While this difference is not insignificant, it can again be attributed to finite Δt and Δx effects, and to the fact that $\omega/\Omega_{ci} = 0.40$ is not much less than unity. In any case, the proper operation of the collisional terms in the code is verified.

4.2. *Plasma Return Currents across a Magnetic Field*

Plasma response to a growing external azimuthal beam current $\mathbf{J}_b = (0, J_{b\theta}, 0)$ perpendicular to an external magnetic field $\mathbf{B} = (0, 0, B_0)$ provides another test of most of the CIDER model and algorithm. This problem is also of importance in ion ring and mirror configurations where energetic particles are to be used to drive the system past field reversal.

It is well known [29–31] that plasma return currents parallel to an external magnetic field cancel any driving beam currents for times less than a magnetic dif-

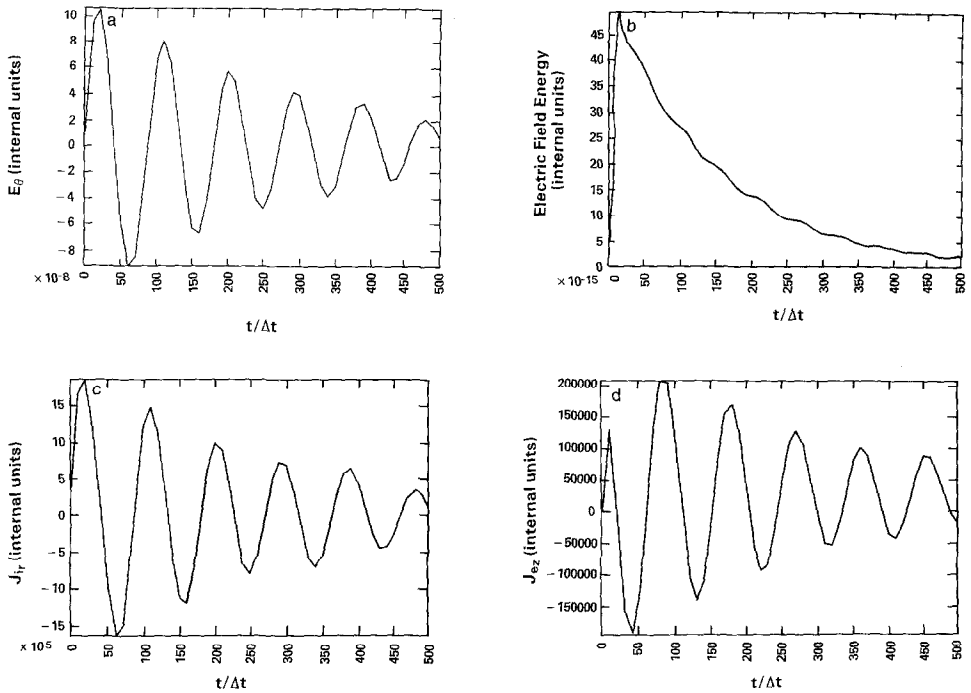

FIG. 6. Damped normal mode test output at $r = z = 1.7$ cm. The extrema do not appear rounded due to a large diagnostic interval. (a) E_θ versus time, (b) electric field energy versus time, (c) radial ion current density versus time, (d) axial electron current density versus time.

fusion time, $\tau_D = 4\pi\sigma a^2/c^2$, where σ is the plasma conductivity and a the characteristic length. However, in the case where the beam current flows across the magnetic field (as is the case for a field-reversing ion ring, e.g.), it has been shown [30, 32, 33] that the plasma response is to cancel the beam current only for times short compared with an Alfvén transit time across the system, $\tau_A \approx r_w/v_A$. This cancellation is due to an azimuthal $\mathbf{E} \times \mathbf{B}$ drift of the electrons; the required radial electric field develops as the ion beam attracts electrons to provide charge neutralization on injection. For times longer than τ_A, however, the return current does not continue to grow, even though the beam current does. Instead, the return current simply oscillates with an amplitude much less than that of the beam current. This result has been explained [2] in terms of destructive interference of Alfvén waves reflecting from the radial wall; the same authors have performed one-dimensional simulations of this effect. Friedman [6] has observed the same result using his multidimensional linearized simulation model.

As was the case with Friedman's simulations [6], the CIDER simulations we are about to describe differ from some of the previous work in several respects. Cylindrical geometry is used. The driving current is represented by an additional term added to the azimuthal velocity average array, so that we ignore the extra electrons

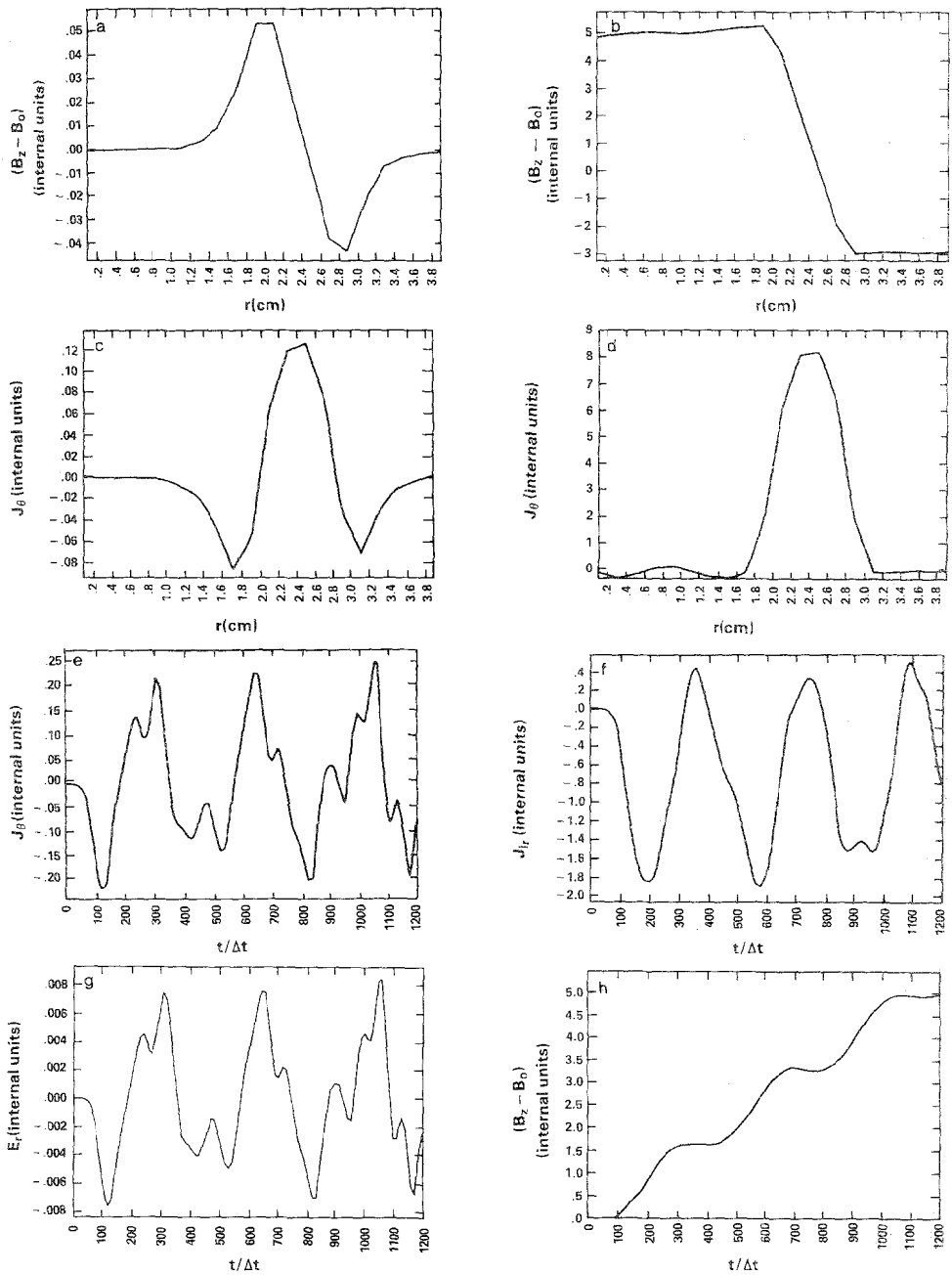

FIG. 7. Return current test output: (a) $(B_z - B_0)$ versus r at $z = 1.7$ cm, $t < \tau_A$, (b) $(B_z - B_0)$ versus r at $z = 1.7$ cm, $t \gg \tau_A$, (c) J_θ versus r at $z = 1.7$ cm, $t < \tau_A$, (d) J_θ versus r at $z = 1.7$ cm, $t \gg \tau_A$, (e) J_θ versus time at $r = 1.1$ cm, $z = 1.7$ cm, (f) radial ion current density versus time at $r = 1.1$ cm, $z = 1.7$ cm, (g) E_r versus time at $r = 1.1$ cm, $z = 1.7$ cm, (h) $(B_z - B_0)$ versus time at $r = 1.1$ cm, $z = 1.7$ cm.

needed to ensure quasineutrality if a beam specie were actually present. The driving current grows linearly in time, but is given a finite radial width to reduce short wavelength-generated noise. In contrast to Friedman's work, however, our simulations are fully nonlinear.

In Figs. 7 we present the results of such a simulation. Parameters were the same

from $r = 1.9$ cm to $r = 2.9$ cm. We take $\partial/\partial z = 0$. Of particular interest are Figs. 7a–d, which show radial profiles of $(B_z - B_0)$ and $J_{\theta_{\text{total}}}$ at $z = 1.7$ cm for both early ($t < \tau_A$) and late ($t \gg \tau_A$) times. At early times, the cancellation effect of the plasma current is evident. However, the field profile at late times is that of the driving current alone, indicating that the plasma return current no longer causes cancellation. Similarly, the radial profile of the total azimuthal current at late times is that of the drive current. (Note that the vertical scales are different at early and late times because the drive current continues to grow linearly.) The time history plots in Figs. 7e–h verify that plasma quantities are oscillatory, while $(B_z - B_0)$ grows in "staircase" fashion as Alfvén waves continually reflect from the outer wall.

5. Conclusions

We have presented a $2\frac{1}{2}$-dimensional (r, z, v_r, v_θ, v_z; $\partial/\partial\theta = 0$) quasineutral hybrid simulation model in which ions are represented by particles and electrons by an inertialess thermal fluid. The model includes a number of effects not heretofore considered, including finite pressure corrections, transport of electron energy, collisions, atomic physics, and radiative energy loss. The model equations are solved by a generalization of the predictor–corrector algorithm originally proposed by Byers *et al.* [2]. The code has been extensively tested and then applied [8] to the problem of propagation of an energetic ion beam through a preformed z-pinch plasma channel.

A number of other features are currently being implemented in CIDER. Most importantly, we have developed a Cartesian version of the code, including more sophisticated electron, collision and ionization models. This version is suitable for studying an entirely new class of problems, such as ion dynamics in the ionosphere. Such simulations will be described in forthcoming publications [34].

APPENDIX: Convergence Analysis

The computation of the electric field from Eq. (12) requires an iteration as discussed in Section 3.1. To examine the convergence of this iteration, we consider first the simplest case which excludes collisions and ion motion. These effects impose additional constraints which will be considered separately.

Under this assumption, the iteration process, based on Eqs. (12) and on Ampère's law, reduces to

$$\mathbf{B}^{(q+1)} = \mathbf{B}^{\text{old}} - \frac{c\Delta t}{2}\nabla \times \mathbf{E}^{(q)}, \tag{A1}$$

$$\mathbf{E}^{(q)} = -\frac{1}{4\pi ne}\mathbf{B}^{(q)} \times (\nabla \times \mathbf{B}^{(q)}), \tag{A2}$$

where the superscripts (q) denote the iteration level and "old" refers to the known value at the previous time step. Combining Eqs. (A1) and (A2) yields

$$\mathbf{B}^{(q+1)} = \mathbf{B}^{\text{old}} + \frac{c\Delta t}{8\pi e}\nabla \times \frac{1}{n}[\mathbf{B}^{(q)} \times (\nabla \times \mathbf{B}^{(q)})]. \tag{A3}$$

Let $\delta\mathbf{B}^q \equiv \mathbf{B}^q - \mathbf{B}^{q-1}$ and $\delta\mathbf{B}^{q+1} \equiv \mathbf{B}^{q+1} - \mathbf{B}^q$ denote two successive corrections. From Eq. (A3),

$$\delta\mathbf{B}^{(q+1)} = \mathbf{B}^{\text{old}} - \mathbf{B}^{(q)} + \frac{c\Delta t}{8\pi e}\nabla \times \frac{1}{n}[\mathbf{B}^{(q)} \times (\nabla \times \mathbf{B}^{(q)})],$$

and expanding the last term in the right member yields

$$\delta\mathbf{B}^{(q+1)} = \mathbf{B}^{\text{old}} - \mathbf{B}^{(q)} + \frac{c\Delta t}{8\pi e}\nabla \times \left[\frac{\mathbf{B}^{(q-1)}}{n} \times [\nabla \times \mathbf{B}^{(q-1)}]\right]$$
$$+ \frac{c\Delta t}{8\pi e}\nabla \times \frac{1}{n}[\mathbf{B}^{(q-1)} \times (\nabla \times \delta\mathbf{B}^{(q)}) + \delta\mathbf{B}^{(q)} \times (\nabla \times \mathbf{B}^{(q-1)})]. \tag{A4}$$

This expansion is justified since $\delta\mathbf{B}^{(q)}$ approaches zero when the iteration converges, and the density, n, does not change since ion motion is not included in this analysis. Note that the first line in Eq. (A4) vanishes identically, and denoting the second line as the linear operator $\mathscr{L}_1(\delta\mathbf{B}^{(q)})$ yields

$$\delta\mathbf{B}^{(q+1)} = \mathscr{L}_1(\delta\mathbf{B}^{(q)}).$$

Since convergence requires $|\delta\mathbf{B}^{(q+1)}| < |\delta\mathbf{B}^{(q)}|$, we must have $|\mathscr{L}_1| < 1$. Assuming $\nabla \simeq \Delta x_{\min}^{-1}$, this condition reduces to

$$n \gtrsim \frac{cB\Delta t}{4\pi e\, \Delta x_{\min}^2} \tag{A5}$$

or

$$\Omega_{\text{ci}}\, \Delta t \lesssim \left[\frac{\omega_{\text{pi}}\, \Delta x_{\min}}{c}\right]^2, \tag{A6}$$

where $\Omega_{\text{ci}} = eB/m_i c$ is the ion cyclotron frequency and $\Delta x_{\min}$ denotes the minimum grid spacing.

The effects of collisions and ion motion are now considered. If $\nu_{\max}$ denotes the dominant collision frequency, the corresponding term in Eq. (12) gives

$$\mathbf{E}^{(q)} = \frac{cm_e \nu_{\max}}{4\pi e^2 n} \nabla \times \mathbf{B}^{(q)}. \tag{A7}$$

Substituting $\mathbf{E}^{(q)}$ from this equation into Eq. (A1) gives

$$\mathbf{B}^{(q+1)} = \mathbf{B}^{\text{old}} + \mathscr{L}_2(\mathbf{B}^{(q)}), \tag{A8}$$

where

$$\mathscr{L}_2(\mathbf{B}^{(q)}) = -\frac{c^2 \Delta t \nu_{\max}}{4\pi e^2} \nabla \times \frac{1}{n} (\nabla \times \mathbf{B}^{(q)}).$$

It follows from (A8) that $\delta\mathbf{B}^{(q+1)} = \mathscr{L}_2(\delta\mathbf{B}^{(q)})$, and convergence requires $|\mathscr{L}_2| < 1$ or

$$\nu_{\max} \Delta t \lesssim \left[\frac{\omega_{pe} \Delta x_{\min}}{c}\right]^2. \tag{A9}$$

Finally, ion motion introduces the operator

$$\mathscr{L}_3(\mathbf{B}^{(q)}) = -\frac{\Delta t}{2} \nabla \times (\langle \mathbf{v}_i \rangle \times \mathbf{B}^{(q)}),$$

and the condition $|\mathscr{L}_3| < 1$ yields

$$\frac{\langle v_i \rangle \Delta t}{2\Delta x} \lesssim 1. \tag{A10}$$

Note that condition (A10) is a Courant condition on the mean ion velocity, but

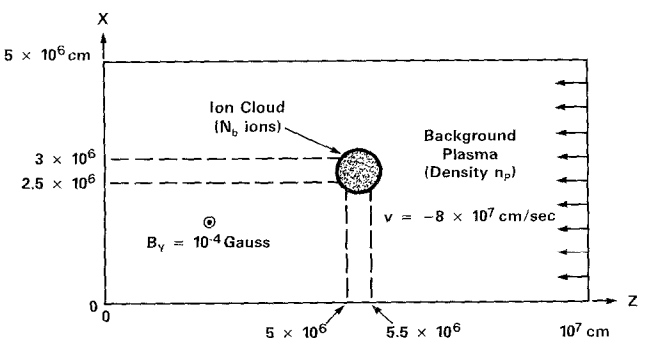

FIG. A1. Initial configuration of the ion cloud and background plasma for convergence tests. The grid has 32 cells in each direction.

TABLE II

Convergence Tests with $B = 10^{-4}$ G, $\Delta t = 2 \times 10^{-3}$ sec, $\Delta x_{min} = 1.67 \times 10^5$ cm, Given the Convergence Condition $n > 36$ cm^{-3} [a]

Run	n_p (cm^{-3})[b]	N_b[c]	Results
1	10	2.5×10^{14}	No convergence at time step 3.
2	100	2.5×10^{15}	Converged in 8–10 iterations at time step 40 Converged in 18–20 iterations at time step 60 Converged in 20–22 iterations at time step 80 Experience with the code has shown that this type of situation soon leads to nonconvergence.
3	1000	2.5×10^{16}	Converged in 6–8 iterations at time step 100; this is considered normal.

Note. N_b/n_p = const. for the three runs.

[a] See inequality (A5).

[b] $n_p \equiv$ background plasma density

[c] $N_b \equiv$ number of ions in ion cloud.

conditions (A6) and (A9) are Neumann conditions relating Δt to Δx^2, typical of diffusion computations, and which must be satisfied in addition to the Alfvén–Courant condition (22). These Neumann conditions are the result of the explicit procedure used here in the field computation. We are currently evaluating techniques for removing these constraints.

A set of simulations was done to verify the convergence condition (A6). These simulations were done with the Cartesian version of the code, operating in the $x - z$ plane as shown in Fig. A1, with $\partial/\partial y = 0$. Ions, representing N_p protons, are initialized with zero velocity in the central region shown, and a background plasma of density n_p is blown on these ions from the right boundary. A uniform magnetic field B_y is initially applied throughout the system. These computations are similar

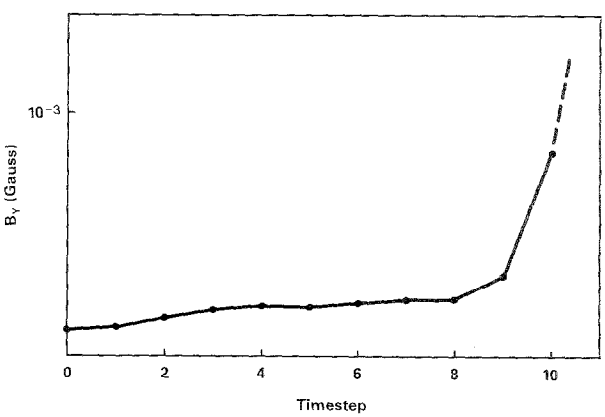

FIG. A2. Magnetic field buildup with $n = 10$ cm^{-3}, $\varepsilon = 10^{-2}$. The iteration fails at time step 11.

to simulation of the interaction of the solar wind with artificial lithium or barium releases in the magnetosphere [34]. With $B_y = 10^{-4}\,G$, (32×32) cells giving $\Delta x_{\min} = 5 \times 10^6/30 = 1.67 \times 10^5$ cm, and $\Delta t = 2 \times 10^{-3}$ sec, condition (A5) gives $n > 36\ \text{cm}^{-3}$.

Three computations were done as shown in Table II, with $\varepsilon = 10^{-6}$ in the convergence test (21). Note that the iteration converged slowly for $n = 100\ \text{cm}^{-3}$ and failed to converge for $n = 10\ \text{cm}^{-3}$. These results are in agreement with the above convergence analysis.

To examine the pathological **B**-fields generated when convergence fails, Run 1 was repeated with $\varepsilon = 10^{-2}$. This allows significant fluctuations of **B** to build up before the iteration fails. The components B_x and B_z parallel to the simulation plane remain zero but the perpendicular component B_y grows gradually from time step 1 to time step 9, and fluctuations build up in the vicinity of the ion cloud. There is a sharp increase in B_y at step 10, see Fig. A2, and at step 11, each iteration gives larger values of B_y until the computation fails due to wild ion motions. A map of B_y at the third iteration of time step 11 is shown in Fig. A3. Note that divergence

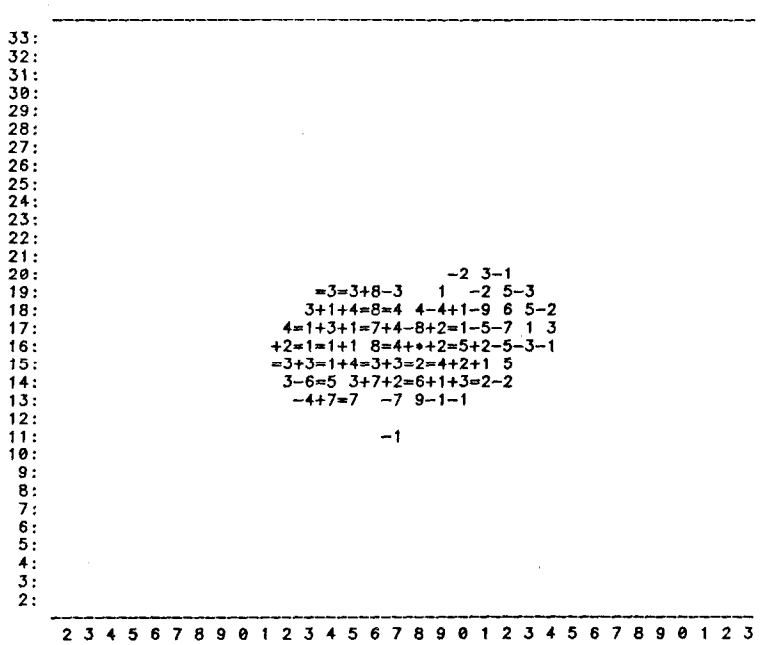

FIG. A3. Map of B_y versus x and z at the third iteration of divergent time step 11. Full scale is $|B_y|_{\max} = 6.15$ G, and the printed values give percentages of full scale as follows:

+5:	45 to 55%,	=5:	−45 to −55%
5:	4.5 to 5.5%,	−5:	−4.5 to −5.5%
+*:	+full scale,	=*:	−full scale.

Blanks are less than 0.5% of full scale.

tuations, justifying the assumption $v = 2x_{min}$ made in deriving the convergence condition (A5).

ACKNOWLEDGMENTS

The authors would like to thank A. Friedman, D. W. Hewett, B. I. Cohen, and A. T. Drobot for many useful discussions. This work was supported by the U.S. Department of Energy.

REFERENCES

1. A. G. SGRO AND C. W. NIELSON, *Phys. Fluids* **19**, 126 (1976).
2. J. A. BYERS, B. I. COHEN, W. C. CONDIT, AND J. D. HANSON, *J. Comput. Phys.* **27**, 363 (1978).
3. D. S. HARNED, *J. Comput. Phys.* **47**, 452 (1982).
4. D. W. HEWETT AND C. W. NIELSON, *J. Comput. Phys.* **29**, 219 (1978).
5. D. W. HEWETT, *J. Comput. Phys.* **38**, 378 (1980).
6. A. FRIEDMAN, R. N. SUDAN, AND J. DENAVIT, *J. Comput. Phys.* **40**, 1 (1981).
7. A. MANKOFSKY, Cornell University Ph.D. thesis, 1982 (unpublished).
8. A. MANKOFSKY AND R. N. SUDAN, *Nucl. Fusion* **29**, 827 (1984).
9. L. SPITZER, *Physics of Fully Ionized Gases* (Interscience, New York, 1962), Chap. 5.
10. B. A. TRUBNIKOV, "Particle Interactions in a Fully Ionized Plasma," in *Reviews of Plasma Physics*, edited by M. A. Leontovich (Consultants Bureau, New York, 1965), Vol. 1, p. 105.
11. S. I. BRAGINSKII, "Transport Processes in a Plasma," in *Reviews of Plasma Physics*, edited by M. A. Leontovich (Consultants Bureau, New York, 1965) Vol. 1, p. 205.
12. D. E. POST, R. V. JENSEN, C. B. TARTER, W. H. GRASBERGER, AND W. A. LOKKE, *Atomic Data and Nuclear Data Tables* **20**, 397 (1977).
13. C. B. TARTER, *J. Quant. Spectrosc. Radiat. Transfer* **17**, 531 (1977).
14. G. ELWERT, *Z. Naturforsch. A* **7**, 432 (1952).
15. R. W. P. MCWHIRTER, "Spectral Intensities," in *Plasma Diagnostic Techniques*, edited by R. H. Huddlestone and S. L. Leonard (Academic Press, New York, 1965), p. 201.
16. C. G. DARWIN, *Philos. Mag.* **39**, 537 (1920).
17. J. D. JACKSON, *Classical Electrodynamics* (Wiley, New York, 1975), 2nd ed., Sect. 12.7.
18. C. W. NIELSON AND H. R. LEWIS, "Particle-Code Models in the Nonradiative Limit," in *Methods in Computational Physics*, edited by B. Alder, S. Fernbach, M. Rotenberg, and J. Killeen (Academic Press, New York, 1976), Vol. 16, p. 367.
19. D. L. BOOK, *NRL Plasma Formulary* (Office of Naval Research, Washington, D.C., 1980), p. 39.
20. J. F. JANNI, Air Force Weapons Laboratory Report AFWL-TR-65-150, 1966 (unpublished).
21. J. F. ZIEGLER AND W. K. CHU, *Atomic Data and Nuclear Data Tables* **13**, 463 (1974).
22. P. M. LYSTER, Laboratory of Plasma Studies, Cornell University, Ithaca, NY, private communication (1984).
23. C. W. NIELSON AND E. L. LINDMAN, in *Proceedings of the Sixth Conference on Numerical Simulation of Plasmas* (Livermore, CA, 1973), p. 148.
24. T. D. ROGNLIEN, in *Proceedings of the Eighth Conference on Numerical Simulation of Plasmas* (Monterey, CA, 1978), paper PA-4.
25. A. T. DROBOT, Science Applications International Corporation, McLean, VA, private communication (1982).
26. I. B. BERNSTEIN AND S. K. TREHAN, *Nucl. Fusion* **1**, 3 (1960).
27. T. H. STIX, *The Theory of Plasma Waves* (Interscience, New York, 1962), Chap. 5.

28. D. MONTGOMERY, *Phys. Fluids* **2**, 585 (1959).
29. D. A. HAMMER AND N. ROSTOKER, *Phys. Fluids* **13**, 1831 (1970).
30. R. E. LEE AND R. N. SUDAN, *Phys. Fluids* **14**, 1213 (1971).
31. K. R. CHU AND N. ROSTOKER, *Phys. Fluids* **16**, 1472 (1973).
32. M. L. ANDREWS *et al.*, in *Plasma Physics and Controlled Nuclear Fusion Research* (International Atomic Energy Agency, Vienna, 1971), Vol. 1, p. 169.
33. H. L. BERK AND L. D. PEARLSTEIN, *Phys. Fluids* **19**, 1831 (1976).
34. C. C. GOODRICH, A. T. Y. LUI, A. MANKOFSKY, AND K. PAPADOPOULOS, *Bull. Amer. Phys. Soc.* **30**, 1468 (1985).